Coupling Uniform Pore Size And Multi-Chemisorption Sites: Hierarchically Ordered Porous Carbon For Ultra-Fast And Large Zinc Ion Storage

Zhongyou Peng, Alexander G. Bannov, Shulong Li, Yuting Huang, Ling Tang, Licheng Tan,* and Yiwang Chen*

Constructing hierarchically ordered macro/meso—microporous structures of carbonaceous cathode with matchable pore size and adequate active sites is significant toward large Zn^{2+} storage, but remains a formidable challenge. Herein, a new perspective is reported for synthesizing phosphorus and nitrogen dual-doped hierarchical ordered porous carbon (PN-HOPC) by eliminating the micropore confinement effect and synchronously introducing multi-chemisorption sites. The interconnected macropore can effectively facilitate long-distance mass transfer, and meso—microporous wall can promote accessibility of active sites. Density functional theory (DFT) calculations identify that the P and N co-doping markedly contributes to the reversible adsorption/desorption of zinc ions and protons. Consequently, the optimized PN-HOPC exhibits outstanding Zn^{2+} storage capabilities in terms of high capacity (211.9 mAh g^{-1}), superb energy density (169.5 Wh kg^{-1}), and ultralong lifespan (99.3% retention after 60 000 cycles). Systematic ex situ measurements integrating with in situ Raman spectroscopy and electrochemical quartz crystal microbalance (EQCM) techniques elucidate that the superior electrochemical capability is ascribed to the synergistic effect of the Zn^{2+}, H^+, and SO_4^{2-} co-adsorption mechanism, as well as invertible chemical adsorption. This study not only provides new insights to design advanced carbon materials toward practical applications but also sheds lights on a deeper understanding of charge storage mechanism for zinc-ion capacitors (ZICs).

1. Introduction

The improving requirements of large-scale energy storage, smart electronics, vehicles, and intermittent renewable energies have inspired researches on novel electrochemical energy storage systems (EESs) that not only offer high energy and power densities, but also possess high safety.[1–7] In this regard, aqueous based EES devices with superior power delivery, high safety and low cost are expected to be one of the hopeful candidates for renewable energy storage.[8–11] Nevertheless, current commercial aqueous EES, such as Pb—acid and Ni—Cd rechargeable batteries subject to low energy density and inferior cycling life,[12,13] which increase the levelized energy cost, thus impeding their further practical applications. Particularly, aqueous zinc ion capacitors (ZICs) combine the advantages of battery-type electrodes with electrochemical redox reactions and capacitor-type electrodes with electrostatic adsorption/desorption. Generally, the reversible zinc plating/stripping process on Zn metal anode can endow battery-like energy density for the ZICs, while the fast ions adsorption/desorption behaviors on the carbon cathode provides supercapacitor-like power density and fast charge/discharge capability.[14,15] Specifically, zinc metal is regarded as a desirable anode for zinc—based energy storage devices on account of its superior theoretical capacity (820 mAh g^{-1}/5855 mAh cm^{-3}), suitable redox potential (−0.76 V vs standard hydrogen electrode (SHE)), and excellent lifespan.[16–19] Theoretically, the reversible Zn^{2+} adsorption/desorption of carbonaceous cathode materials without phase transition possesses limitless cycle life. Thus, it is vital to develop compatible carbon cathode materials to match Zn anodes for achieving the desired Zn^{2+} storage capabilities.

Recently, various carbonaceous cathode materials, such as activated carbon,[20,21] biomass—derived carbon,[22,23] pyrolytic carbon,[24–26] carbon nanotubes,[27,28] and graphene[29,30] with the pore architectures and tunable chemical properties have been designed for ZICs. However, these carbonaceous materials mainly possess porous structures with the mismatch of pore sizes with charge carriers, random pore size distribution, and low connectivity of mesopores and/or macropores, thereby

Z. Peng, S. Li, Y. Huang, L. Tang, L. Tan, Y. Chen
College of Chemistry and Chemical Engineering/Institute of Polymers and Energy Chemistry (IPEC)/Jiangxi Provincial Key Laboratory of New Energy Chemistry
Nanchang University
999 Xuefu Avenue, Nanchang 330031, China
E-mail: tanlicheng@ncu.edu.cn; ywchen@ncu.edu.cn

A. G. Bannov
Department of Chemistry and Chemical Engineering
Novosibirsk State Technical University
K. Marx 20, Novosibirsk 630073, Russia

Y. Chen
National Engineering Research Center for Carbohydrate Synthesis/Key Laboratory of Fluorine and Silicon for Energy Materials and Chemistry of Ministry of Education
Jiangxi Normal University
99 Ziyang Avenue, Nanchang 330022, China

bringing about unsatisfactory Zn^{2+} storage capability and sluggish charge transfer kinetics, further leading to unsatisfied energy density and poor cyclic stability of ZICs. As acknowledged, Zn^{2+} could interacts intensely with circumambient water molecules to generate hexahydrate structure ($[Zn(H_2O)_6]^{2+}$) with the size of charge-carrier ions expansion from 1.48 to 8.6 Å in aqueous electrolytes.[31,32] The inaccessibility of solvated $[Zn(H_2O)_6]^{2+}$ ions in micropores will lead to a serious loss of the charge density, unit surface area utilization, and energy storage capacity due to ion-sieving effects.[33,34] Therefore, the rational design of hierarchically macro/meso−microporous structure of carbon material with matchable pore size, efficient electron/ion transport, and adequately exposed active sites is significant toward densely and neatly packing Zn^{2+} storage. Highly ordered macro/meso−microporous are ordinarily introduced into carbon materials via hard-template methods.[21] However, it is difficult to control the growth process of carbon materials with confined space, and it is still challenging to synthesize hierarchical porous materials with highly ordered structure. To further enhance Zn^{2+} storage capability, the introduction of heteroatoms, such as of boron,[35,36] phosphorus,[24,25] nitrogen,[25,37,38] sulfur[39] and oxygen[12,40] is an effective strategy to provide more redox active sites and increase additional pseudo capacitance by the chemical adsorption/desorption of Zn^{2+}.[23] Meanwhile, the heteroatom dopants can change the surface chemical properties and modulate charge storage behavior of carbon cathodes, and thus providing adequate Zn^{2+} storage active sites and further optimizing the performance of ZICs. Nevertheless, heteroatoms are difficult to dope into carbon skeletons uniformly to adjust their electronic structures, so as to form active sites in carbon cages, which is not conducive to mass transport during operation.[24] Currently, despite plenty of advances in porous carbon materials, few basic researches have concentrated on the improved mechanism of heteroatom dopants for efficient Zn^{2+} storage, especially the impact of the uniform pore structures and doping type on the electrochemical properties. Moreover, the charge storage mechanism of carbonic cathodes in ZICs is still in its infancy and not well elucidated yet. Therefore, it is imminent to profoundly illustrate the charge storage mechanism of ZICs, which is favorable to precisely design carbon cathodes and optimize electrochemical performance of devices.

Herein, we present new perspectives to improve the Zn^{2+} storage capabilities of the phosphorus and nitrogen dual-doped hierarchical ordered porous carbon (PN-HOPC) via eliminating the micropore confinement effect and introducing multiple chemisorption sites. The optimized PN-HOPC with uniform and matchable pore size profitably accommodating solvated Zn^{2+}, rich heteroatom (P, N, O) doping, and abundant chemisorption sites is conducive to efficient Zn^{2+} storage. Importantly, marriage of experimental characterizations and density function theory (DFT) calculation identify that the P and N co-doping markedly reduce the energy barrier of the Zn^{2+} absorption and significantly facilitate electron transfer behavior. As a result, the as-assembled ZIC with PN-HOPC cathode shows specific capacity as high as 211.9 mAh g^{-1}, exceptional energy density of 169.5 Wh kg^{-1}, super power density of 64.0 kW kg^{-1}, and long service life of 99.3% capacity retention (over 60 000 cycles). Besides, systematic ex situ measurements, in situ Raman spectroscopy and electrochemical quartz crystal microbalance (EQCM) techniques testify that the

outstanding Zn^{2+} storage capabilities are ascribed to the synergic effect of the Zn^{2+}, H^+, and SO_4^{2-} co-adsorption as well as reversible chemical adsorption. Moreover, the quasi-solid-state ZIC exhibits low self-discharge rate and ultralong cyclic life of up to 50 000 cycles (96.8% capacity retention), suggesting great potential in energy storage systems. These glorious properties strongly exhibit the effectiveness and appropriateness of the proposed new insights into coupling pore size and multi-chemisorption sites of carbon materials to enhance the Zn^{2+} storage capability of ZICs.

2. Results and Discussion

The synthesis process of the PN-HOPC is schematically illustrated in **Figure 1**a. Briefly, a saturated methanolic solution comprising 2-methylimidazole and $Zn(NO_3)_2 \cdot 6H_2O$ was added into 3D ordered polystyrene spheres (PS) templates with a diameter size of 250 nm (Figure S1, Supporting Information), and then a blended $CH_3OH/NH_3 \cdot H_2O$ solution was applied to induce the generation of ZIF-8 crystalline phase (ZIF-8@PS) (Figure S2, Supporting Information). Afterward, the 3D ordered macro-microporous ZIF-8 (3DOM-ZIF-8) (Figure S3, Supporting Information) was fabricated via eliminating the PS templates and 3DOM-ZIF-8 was carbonized to acquire the nitrogen doped hierarchical ordered porous carbon (N-HOPC) with well-defined polyhedral morphology (Figures S4, S5, Supporting Information). Finally, the N-HOPC was mixed with phytic acid, and the PN-HOPC was synthesized via heat treatment to realize simultaneous activation and phosphorization within a one-step process. It is worth mentioning that the use of tiny amounts of phytic acid can not only avoid large-scale utilization of harmful PH_3 carrier system, but also create a closed vapor environment.[24] Scanning electron microscopy (SEM) and transmission electron microscopy (TEM) images of PN-HOPC (Figure 1b–e) display high uniformity and ordered interconnected macropores with the average diameter of ≈180 nm and the wall thickness of ≈40 nm. Moreover, abundant mesopores can be formed onto the circumambient walls, which lead to the tight contact of the PS spheres preventing the methanolic precursor from penetrating the contact point and remaining holes after the PS elimination.[41] The entire 3D skeleton of PN-HOPC with mesopores on the circumambient walls retains the continuous channels, which can shorten the distance of ion mobility, and facilitate the charge transfer process for reversible ion physical/chemical adsorption/desorption. From the high-resolution TEM (HRTEM) (Figure 1f,g), PN-HOPC displays characteristic of amorphous carbon with disordered nanopores. Besides, the element mapping images (Figure 1h) indicate the P and N elements uniformly distributed in the whole PN-HOPC. As a comparison, the nitrogen doped porous carbon (N-PC) (Figure S6a, b, Supporting Information) and phosphorus, nitrogen dual-doped porous carbon (PN-PC) (Figure S6c,d, Supporting Information) without employing the PS template were also fabricated by carbonizing the ZIF-8.

X-ray diffraction (XRD) of the N-PC, N-HOPC, and PN-HOPC samples indicate two broad peaks at 2θ ≈24.6° and 44.0° (**Figure 2**a), which are related to (002) and (100) planes of graphite carbon, respectively.[24,42] Weak left shift was observed for PN-HOPC, suggesting that P doping can expand the interlayer distance of carbon layers, which is beneficial to the fast diffusion of the
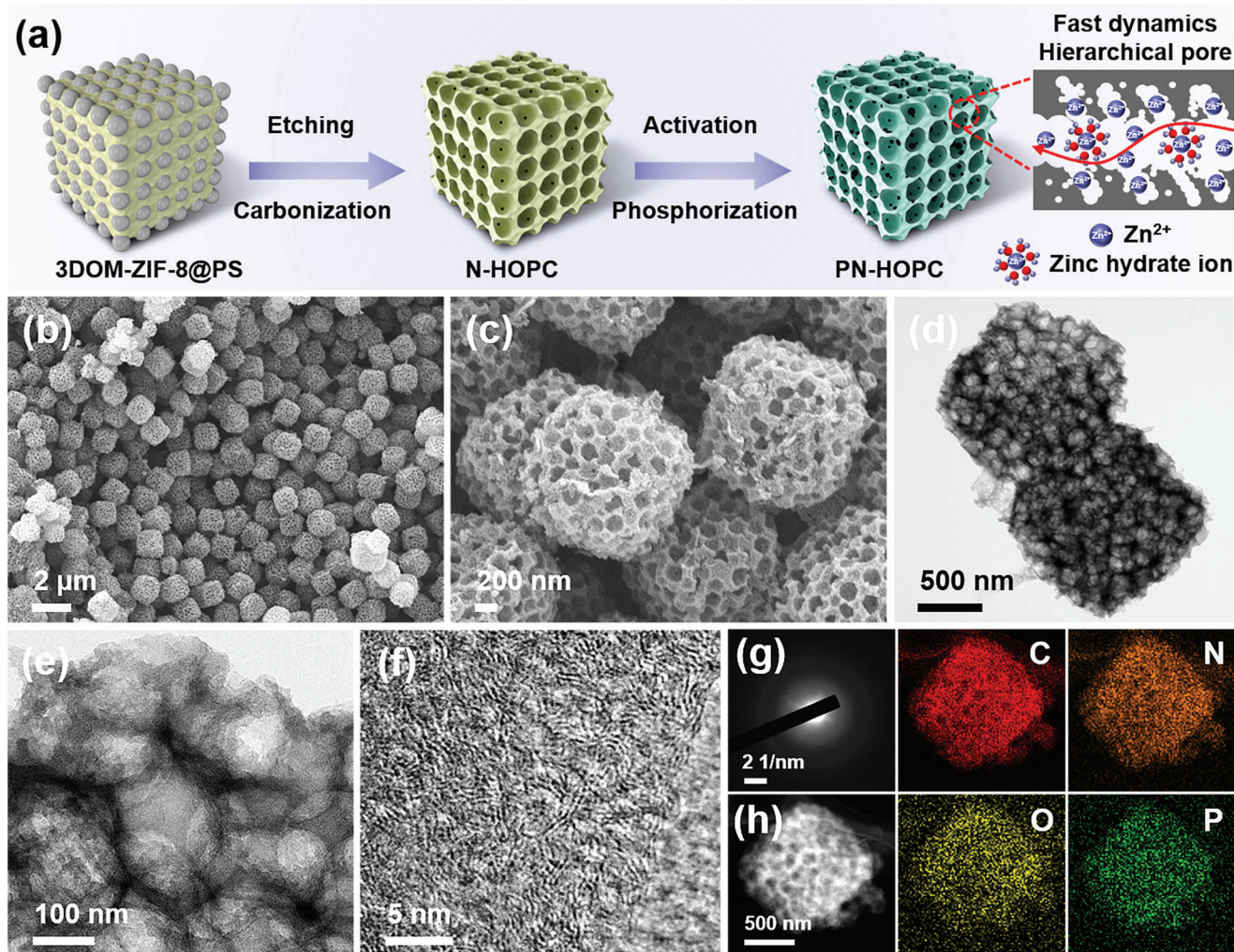
**ADVANCED
SCIENCE NEWS**

www.advancedsciencenews.com

**ADVANCED
FUNCTIONAL
MATERIALS**

www.afm-journal.de

Figure 1. a) Schematic illustration of the formation process of PN-HOPC. b, c) SEM, d, e) TEM, f) HRTEM, g) selected area electron diffraction (SAED) images, and h) corresponding elemental mapping of PN-HOPC.

Zn^{2+}. The Raman spectra exhibit two peaks situated ≈1340 (D-band) and 1580 cm^{-1} (G-band), attributing to the defective carbon and sp^2-hybridized graphitic carbon, respectively (Figure S7a–c, Supporting Information). Moreover, the peak area ratio (I_D/I_G) of PN-HOPC shows a large value of 4.4, implying the plentiful defects and high degree of disorder in graphitic lattices.[26] The I_D/I_G value reflects that PN-HOPC has high-density defects (Figure S7d, Supporting Information), which can offer abundant Zn^{2+} storage sites and enhance Zn^{2+} storage capability. The porous character of the N-PC, N-HOPC, and PN-HOPC samples were confirmed by the nitrogen adsorption-desorption measurement. The combined I/IV-type isotherm shows the high nitrogen adsorption at lower pressure and the typical hysteresis loop, demonstrating the coexistence of mesopores and micropores (Figure 2b).[43] In addition, the hierarchically porous structure is also verified via the pore size distribution with the aperture distributions at ≈0.9, 3.2, and 5.0 nm (Figure 2c), which could provide efficient channels for the bare Zn^{2+} (1.48 Å) and $[Zn(H_2O)_6]^{2+}$ (0.86 nm) transport. The PN-HOPC sample displays a high specific surface area (SSA) (1701.8 m^2 g^{-1}) with a

pore volume of 1.29 cm^3 g^{-1}, which are higher than those of N-HOPC (642.4 m^2 g^{-1} and 0.58 cm^3 g^{-1}) and N-PC (493.7 m^2 g^{-1} and 0.27 cm^3 g^{-1}) with dominantly microporous structure. Besides, PN-HOPC demonstrates a high proportion of mesopores (S_{meso}/S_{BET} = 32.2%) (Table S1, Supporting Information), which can not only facilitate electrolyte penetration and accelerate electron transfer behavior but also offer abundant active sites for enhancing the energy density.

The X-ray photoelectron spectroscopy (XPS) is used to reveal the surface elemental composition and electronic state of N-PC, N-HOPC, and PN-HOPC samples. The comparing survey spectra (Figure S8a, Supporting Information) confirm the existence of C, O, N, and P elements in PN-HOPC and the content of P and N elements can reach 4.70 and 6.67 at% for PN-HOPC, respectively (Table S2, Supporting Information). The C 1s spectrum of PN-HOPC (Figure 2d) ascribes to five components of related to carbon with different chemical surrounding C-C/C = C (284.4 eV), C-P (285.1 eV), C-N (285.6 eV), C-O (286.4 eV) and C = O (288.3 eV), further displaying the successful doping of phosphorus and nitrogen atoms into the PN-
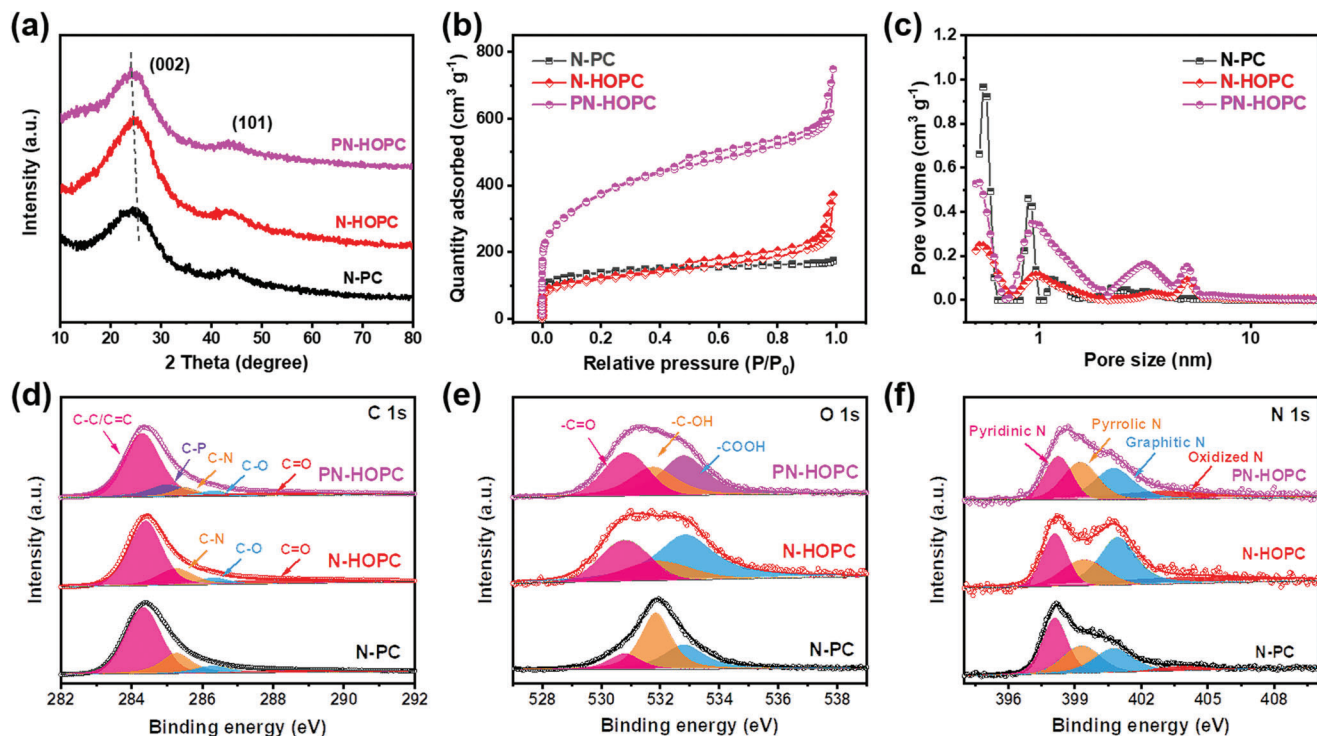
Figure 2. a) XRD patterns, b) Nitrogen adsorption/desorption isotherms, c) pore-size distributions of N-PC, N-HOPC, and PN-HOPC. Core-level d) C 1s, e) O 1s, and f) N 1s XPS spectra of N-PC, N-HOPC, and PN-HOPC.

HOPC. The O 1s spectrum of PN-HOPC (Figure 2e) is resolved into three typical peaks: C = O (530.9 eV), C-OH (531.8 eV), and COOH (532.9 eV).[12] Particularly, PN-HOPC reveals a large content of carbonyl groups (C = O), which can benefit to strengthen the chemical adsorption and accelerate the penetration of electrolytes. The N 1s spectra (Figure 2f) can be assigned to four peaks located at pyridinic-N (398.3 eV), pyrrolic-N (399.3 eV), graphitic-N (400.8 eV), and oxidized-N (403.2 eV).[24,44] Moreover, the presence of P-C (133.5 eV) and P-O (132.5 eV) peaks in P 2p spectrum (Figure S8b, Supporting Information) further confirm the doping of P heteroatom into the porous carbon.[25] The P, N co-doping heteroatoms not only boost the available active sites but also modulate charge distribution of PN-HOPC. Besides, the contact angle measurements verified the improved wettability of PN-HOPC (Figure S9, Supporting Information) with hierarchical porosity and P, N dual-doped, which would increase the zinc ion accessibility and reduce interfacial resistance.

The electrochemical properties of the N-PC, N-HOPC, PN-PC, and PN-HOPC were evaluated as cathode materials for ZICs. Evidently, the cyclic voltammetry (CV) curves exhibit a wide potential difference between Zn anode and PN-HOPC cathode (**Figure 3**a). The Zn anode curve shows the strong redox peaks at −1.2/−0.85 V (vs standard calomel electrode), which assigns to the Zn/Zn^{2+} plating/stripping process.[45] For PN-HOPC cathode, a regular rectangle-like CV curve was observed, representing the outstanding capacitive performance. Remarkably, PN-HOPC ZIC shows the largest the peak intensity and integrated area from the CV curves at 10 mV s$^{−1}$ (Figure 3b), implying its biggest specific capacity. Moreover, the galvanostatic charge–discharge (GCD) curves at 0.2 A g$^{−1}$ exhibit that the PN-HOPC

endows a best-in-class discharge capacity (211.9 mAh g$^{−1}$), surpassing those of PN-PC ZIC (180.2 mAh g$^{−1}$), N-HOPC ZIC (149.9 mAh g$^{−1}$), and N-PC ZIC (138.5 mAh g$^{−1}$) (Figure 3c). In addition, the PN-HOPC still maintains a highly reversible capacity of 94.5 mAh g$^{−1}$ even at an ultrahigh rate of 80 A g$^{−1}$, revealing its excellent structural stability and large-current tolerance (Figure 3d; Figure S10, Supporting Information). The PN-HOPC ZIC exhibits higher capability and rate performance than most of reported carbonaceous cathodes for ZICs[12,21,22,35,39,46,47] (Figure 3e) and AC-based ZIC (Figure S11, Supporting Information), which ascribe to the high porosity and massive P, N, O chemisorption sites of PN-HOPC. In order to further estimate its practical application potential, PN-HOPC ZICs with high quality loadings were studied. Obviously, the discharge specific capacities are 211.9, 174.9, 157.2, 134.0, 107.2, and 87.7 mAh g$^{−1}$ under quality loadings of 1, 3, 5, 10, 20, and 40 mg cm$^{−2}$, respectively (Figure 3f). The outstanding electrochemical property under high quality loading is ascribed to the hierarchically interconnected porous structure of PN-HOPC with short charge/ion diffusion pathways and rapid charge-transfer kinetics. The PN-HOPC ZIC delivers an impressive energy density of 169.5 Wh kg$^{−1}$ and a power density of 64.0 kW kg$^{−1}$, preceding to most of carbon-based ZICs reported[21,29,35–37,39,46] (Figure 3g). More encouragingly, the PN-HOPC ZIC discloses a high capacity of 132.2 mAh g$^{−1}$ at 10 A g$^{−1}$ and long-term cycling life with a 99.3% capacity retention over 60 000 charge/discharge cycles (Figure 3h). Moreover, the PN-HOPC ZIC with the high mass loading of 10 mg cm$^{−2}$ also delivers specific capacity of 68.8 mAh g$^{−1}$ at 5 A g$^{−1}$ and remarkable cycling stability (Figure S12, Supporting Information). The stability of the PN-HOPC cathode and Zn anode was
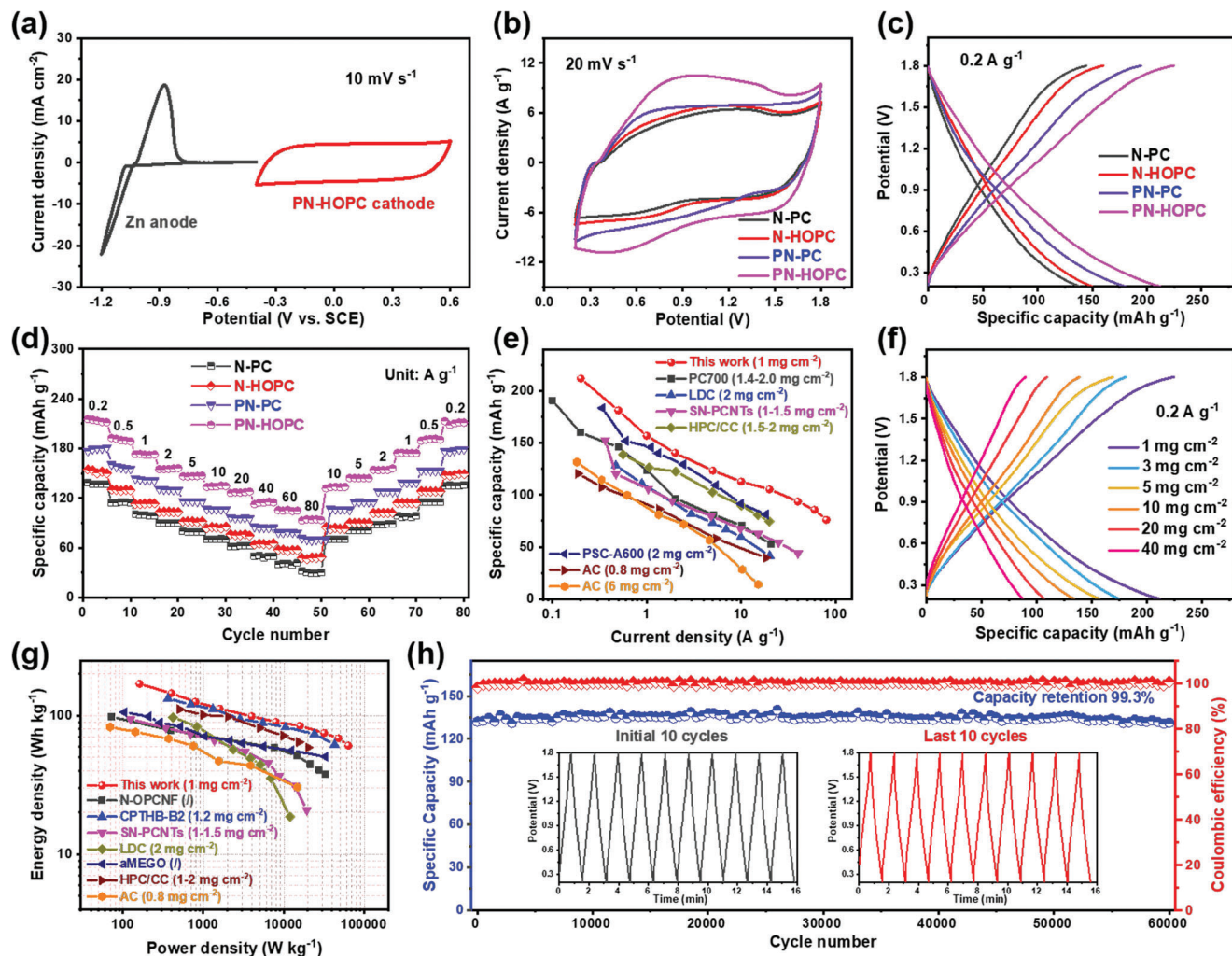
ADVANCED
SCIENCE NEWS
www.advancedsciencenews.com

ADVANCED
FUNCTIONAL
MATERIALS
www.afm-journal.de

Figure 3. a) CV profiles of PN-HOPC cathode and Zn anode at 10 mV s^{-1}. b) CV curves at 10 mV s^{-1}, c) GCD curves at 0.2 A g^{-1}, and d) specific capacities under different current densities of ZICs. e) Rate performance of PN-HOPC ZIC compared with reported ZICs. f) GCD curves of PN-HOPC ZIC at various mass loadings. g) Ragone plots of PN-HOPC ZIC and other recently reported ZICs. h) Cycling stability of PN-HOPC ZIC at 10 A g^{-1}. The insets display GCD curves of initial ten cycles and last ten cycles.

further verified by SEM characterizations before and after cycling (Figures S13, S14, Supporting Information). Interestingly, the Zn metal anode still demonstrates the representative surface morphology of Zn deposition/stripping with no obvious Zn dendrites and byproducts (Figure S14a,b, Supporting Information). Meanwhile, the morphology of PN-HOPC was preserved well after 60 000 cycles (Figure S14c,d, Supporting Information), which further verifies the glorious cycling stability of PN-HOPC ZIC. To highlight the merits of PN-HOPC, the electrochemical performances of PN-HOPC ZIC were compared with the previously reported results (Table S3, Supporting Information), which suggests that PN-HOPC ZIC possesses apparent advantages in terms of power and energy density as well as cycle stability.

The zinc storage kinetics and charge-storage contribution of PN-HOPC were investigated by CV curves (**Figure 4**a). The CV curves of PN-HOPC ZIC show representative redox peaks, signifying the coexistence of charge storage mechanisms from electrical double-layer adsorption/desorption and P-/N-/O-induced

pseudocapacitive response. Furthermore, the capacitive and diffusion behavior contributions can be quantified by the equation of $i = av^b$, where i is the peak current and v is sweep rate, as well as a and b are constants.[12,48] Specially, the b value of 0.5 manifests sluggish diffusion behavior, while the b value of 1.0 attributes to surface capacitance dominated reaction. Obviously, the b values for PN-HOPC cathode (Figure 4b) are calculated to be 0.907 (the reduction peaks) and 0.926 (the oxidization peaks), implying that the electrochemical reactions are determined via ultrarapid capacitive process. The contribution ratio of fast and sluggish reaction kinetics can be calculated via the formula of $i = k_1 v + k_2 v^{1/2}$, where k_1 and k_2 are constants, and $k_1 v$ and $k_2 v^{1/2}$ represent the capacitive and diffusion-controlled processes, respectively.[23,49] Particularly, the ultrarapid capacitive contribution of PN-HOPC cathode at 10 mV s^{-1} reaches 71.7% (Figure S15, Supporting Information). Obviously, diffusion-controlled reactions take place in the high and low potential, which suggests that the charge storage mechanism are Faradaic response.[12] Moreover, the fast
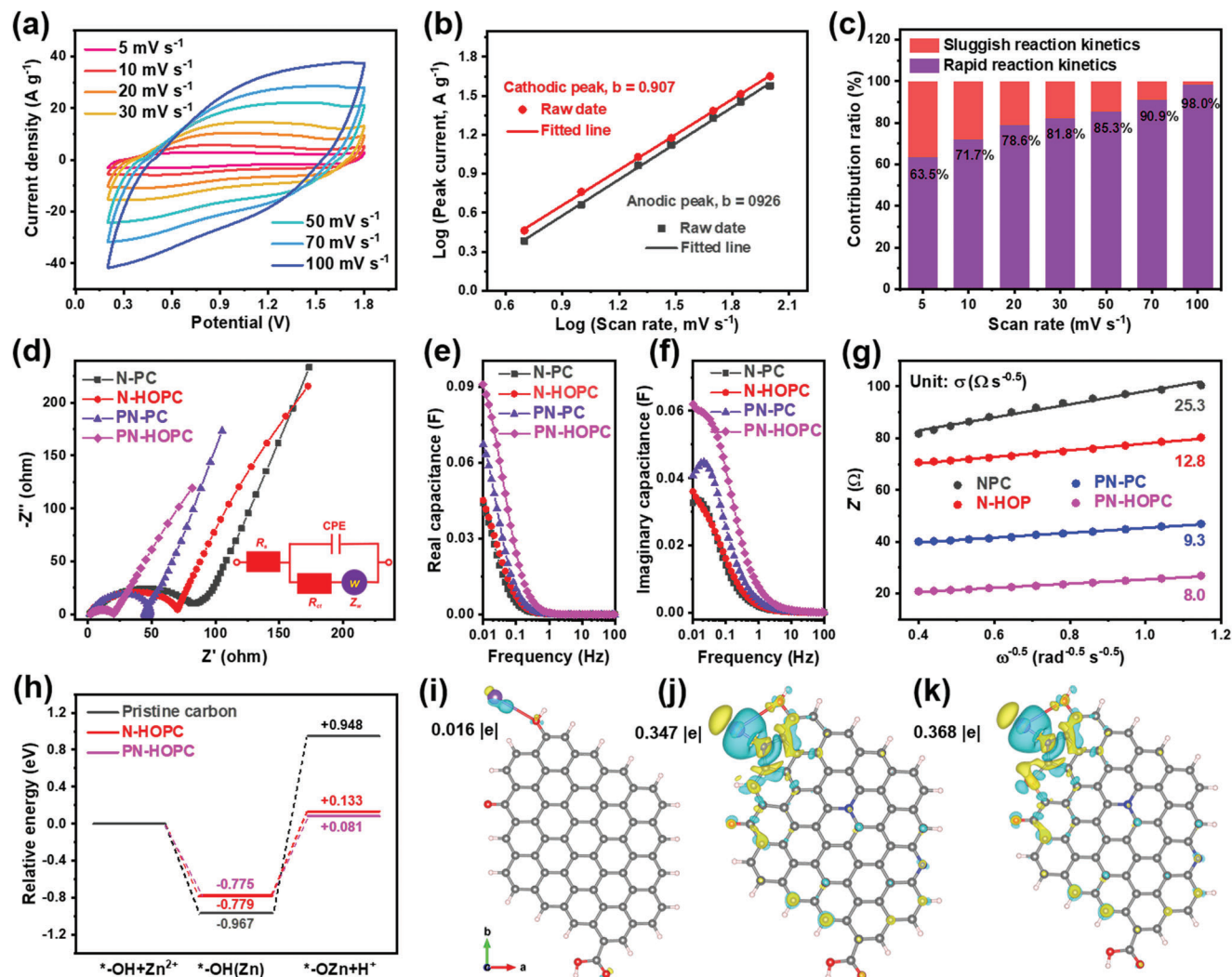
ADVANCED
SCIENCE NEWS
www.advancedsciencenews.com

ADVANCED
FUNCTIONAL
MATERIALS
www.afm-journal.de

Figure 4. a) CV curves of PN-HOPC ZIC. b) Linear relationships between peak currents and sweep rates. c) Normalized contribution ratio of rapid capacitive process at different scan rates. d) EIS spectra and simulating equivalent circuit. e) Real capacitance and f) imaginary capacitance versus frequency. g) The relationship between Z' and $\omega^{-0.5}$. h) Relative energy values of the reaction process. The differential charge density of Zn adsorption on the i) pristine carbon, j) N-HOPC and k) PN-HOPC. Cyan and yellow regions indicate charge depletion and accumulation, respectively. The gray, blue, orange, red, purple, and pink color represents C, N, P, O, Zn, and H atom, respectively.

capacitive contribution gradually increases from 63.5% to 98.0% with the increment of scan rate from 5 to 100 mV s^{-1} (Figure 4c), which is bigger than PN-PC (Figure S16, Supporting Information), N-HOPC (Figure S17, Supporting Information), and N-PC (Figure S18, Supporting Information), demonstrating the capacitive-dominant behavior and fast electrochemical kinetics of PN-HOPC under high scan rates. Electrochemical impedance spectroscopy (EIS) test was employed to evaluate the ion transport and charge transfer kinetics of PN-HOPC. The Nyquist plot of PN-HOPC shows the smallest charge transfer resistance than those of NP-PC, N-HOPC, and N-PC (Figure 4d), indicating the enhanced charge transfer ability and more efficient Zn ion diffusion after luxuriant P and N co-doping. More importantly, a typical complex model of the capacitance was used to survey the capacitance variations, with the real capacitance ($C'(\omega)$) and the imaginary capacitance ($C''(\omega)$) acquiring from EIS data according

to $C(\omega) = C'(\omega) + jC''(\omega)$.[50,51] The PN-HOPC ZIC displays the highest $C'(\omega)$ value (91 mF), further confirming the fast reaction kinetics and excellent capacitive capability (Figure 4e). Moreover, PN-HOPC ZIC possesses the $C''(\omega)$ value of 62 mF and decreased relaxation time constant (τ_0) ($\tau_0 = 1/f$, f corresponds to corresponding to the maximum imaginary part $C''(\omega)$) (Figure 4f), revealing quick Zn ion diffusion and high-rate capability. The faster Zn^{2+} diffusion in PN-HOPC is also verified via the lower Warburg coefficient (σ) (Figure 4g). Meanwhile, the calculated Zn^{2+} diffusion coefficient (D) of PN-HOPC (1.38 × 10^{-10} cm^2 s^{-1}) is higher than those of NP-PC (1.02 × 10^{-10} cm^2 s^{-1}), N-HOPC (5.39 × 10^{-11} cm^2 s^{-1}), and N-PC (1.38 × 10^{-11} cm^2 s^{-1}). These inspiring results reveal that the PN-HOPC electrode exhibits rapid dynamics and more active sites for Zn^{2+} storage.

Additionally, DFT calculations were conducted to further disclose the effect of the heteroatom doped and determine specific
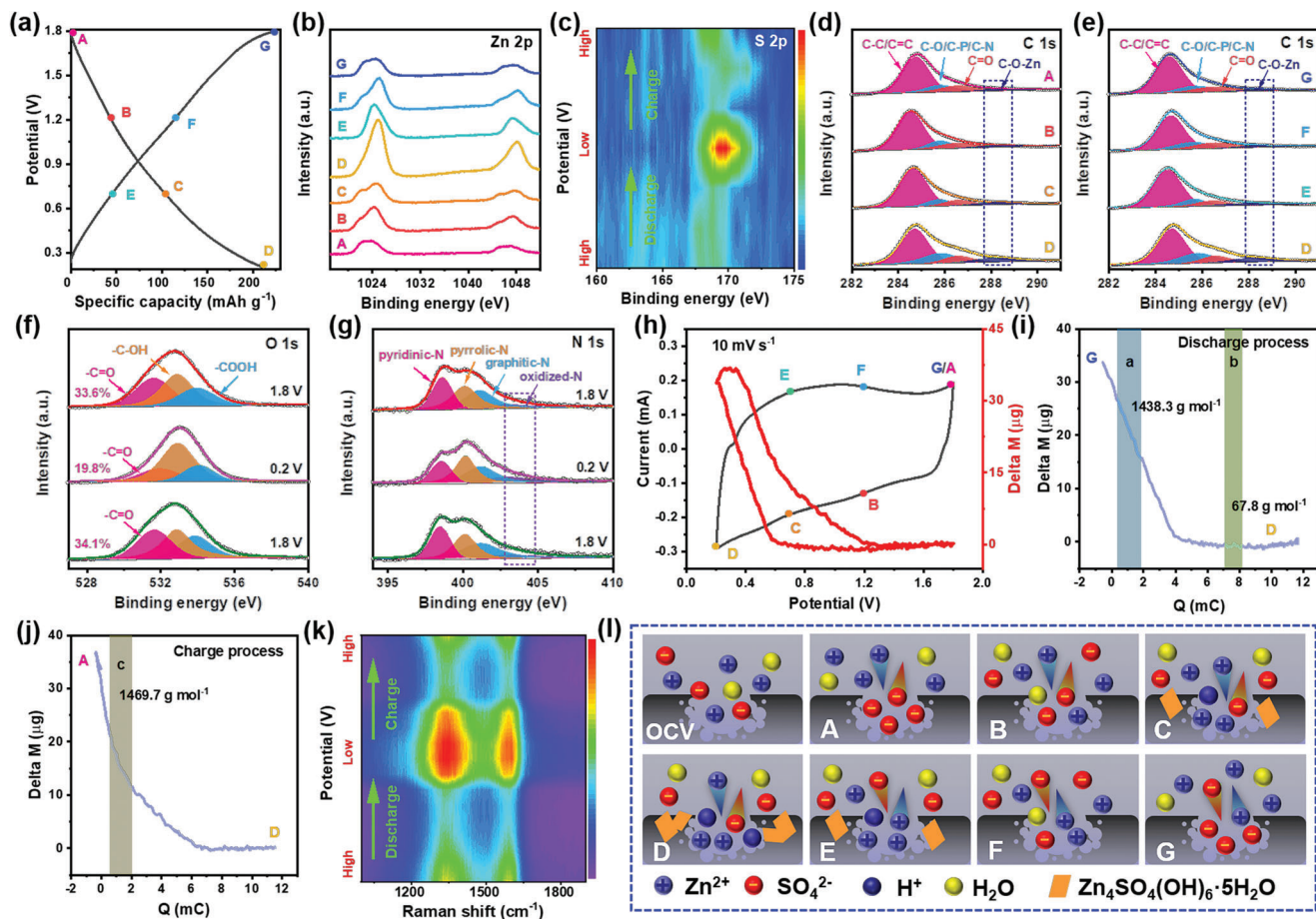
Figure 5. a) The typical GCD curve at 0.2 A g^{-1} and ex situ b) Zn 2p, c) S 2p, d, e) C 1s, f) O 1s, and g) N 1s XPS spectra of PN-HOPC cathode. h) EQCM result of PN-HOPC cathode 10 mV s^{-1}. Mass change versus charge curves during i) discharge and j) charge processes. k) Contour type in situ Raman spectra of PN-HOPC. l) Schematic diagrams of the charge storage mechanism for PN-HOPC cathode.

active sites on the adsorption/desorption of Zn^{2+}. The geometric structures of pristine carbon, N-HOPC and PN-HOPC models were optimized, and the corresponding adsorption energy (ΔE_a) of Zn^{2+} cation was calculated (Figures S19, S20, Supporting Information). Encouragingly, the lower adsorption energy demonstrates that P, N co-doping can significantly improve the adsorption capability of Zn^{2+}. Figure 4h shows the reaction path graph of Zn^{2+} on the cathode surface at the discharging state. First, Zn^{2+} are absorbed on the O active site of -OH group together with a total energy decline. Second, O–H bond is interrupted to produce the C–O–Zn bond and release free H$^+$. In the entire chemical adsorption process, the formation of the C–O–Zn bond is the rate-determining step of reaction. The entire reaction needs to overcome energy barrier of 1.916, 0.912, and 0.857 eV on the non-doped, N-doped and P, N dual-doped electrodes, respectively, which indicates that the PN-HOPC is conducive to the chemical adsorption of Zn^{2+}.[39,51] Besides, the electron transfer behavior is further proved via the charge density difference analysis after Zn^{2+} adsorption (Figure 4i–k). Noteworthily, the charge depletion and accumulation are primarily on Zn and P/N/O adsorption sites, which demonstrates that the P, N co-doping electrode can gain more charge (0.368 |e|) from Zn than the N-doped electrode (0.347 |e|) and non-doped electrode (0.016 |e|), repre-

senting boosted electrochemical energy-storage capability.[25,52,53] Combined with these results, it could be deduced that the introduction of P and N atoms can offer rich chemisorption sites and enhance electron conduction of the PN-HOPC. The excellent electrochemical property of PN-HOPC could originate from its hierarchically ordered porous structures and surface chemistries: i) The conductive and stable 3D architecture with hierarchically porous structure can offer luxuriant active sites and guarantee rapid ion permeation, which is favored for efficient Zn^{2+} storage; ii) The hierarchically porous structure could optimize the transport kinetics for large hydrated Zn^{2+} radius and mitigate volume change, favoring for enhancing capacity, rate capability and cycling stability; iii) The integration of P and N co-doping could decrease the adsorption energy barrier of Zn ions to promote the chemical adsorption capability of Zn^{2+} on the cathode surface.

To better comprehend the charge storage mechanism and elucidate the excellent electrochemical performance of PN-HOPC material, a series of ex situ tests were executed during charge/discharge processes (**Figure 5**a). First, the flaky Zn$_4$SO$_4$(OH)$_6$·5H$_2$O nanosheets (JCPDS No. 39–0688) gradually boost during the discharge process (from A to D), whereas they show the exact opposite process during the charge process (from D to G) (Figure S21, Supporting Information). The TEM ele-

ADVANCED
SCIENCE NEWS
www.advancedsciencenews.com

ADVANCED
FUNCTIONAL
MATERIALS
www.afm-journal.de

ment mapping images reveal that C, O, N, P, Zn, and S elements are spread uniformly (Figures S22, S23, Supporting Information), confirming that $Zn_4SO_4(OH)_6·5H_2O$ can be likely produced during the discharge processes and partially disappeared during the charge processes. Meanwhile, the reversible generation/dissolution of $Zn_4SO_4(OH)_6·5H_2O$ by-products on PN-HOPC cathode surface are also demonstrated from ex situ XRD patterns during the discharge/charge processes (Figure S24, Supporting Information), which reveals that the active sites on the PN-HOPC were hardly damaged. Notably, the adsorption/desorption of H^+ on PN-HOPC cathode surface is inevitable, which will change pH value of the $ZnSO_4$ electrolyte during discharge process. The ex situ SEM images (Figure S25, Supporting Information) exhibit a nanosheet morphology and no zinc dendrites growth on Zn metal surface. The ex situ XRD patterns of Zn foils (Figure S26, Supporting Information) exhibit no obvious impurity peak, further manifesting the highly reversible plating/striping process of Zn^{2+} and the favorable stability of Zn anode. Furthermore, the ex situ XPS was further used to investigate the chemical conversion of the PN-HOPC material at various potential states (Figure S27, Supporting Information). The Zn 2p signal gradually enhances during the discharging process on account of promoted ion adsorption on the carbon surface and almost disappear during the charging process (Figure 5b). Moreover, the intensity of S 2p shows the highest content at state D (Figure 5c), ascribing to the generation of $Zn_4SO_4(OH)_6·5H_2O$ during the discharge processes. Noteworthily, the intensity of S 2p continuously decreases form states D to F, suggesting that the $Zn_4SO_4(OH)_6·5H_2O$ is gradually dissolved during the charge processes. Interestingly, the intensity of S 2p at state G is larger than state F, which demonstrates that the adsorption/desorption of SO_4^{2-} anion mainly occurred at high voltages. The pH test was further conducted to investigate the change of electrolyte pH value during charge/discharge processes (Figures S28–S31, Supporting Information). The color change of the $ZnSO_4$ electrolyte is attributed to reversible Zn^{2+}/H^+ adsorption/desorption on the PN-HOPC cathode during charge/discharge processes. Thus, the formation and dissolution of $Zn_4SO_4(OH)_6·5H_2O$ flakes on the PN-HOPC cathode is related to the change of electrolyte pH value during charge/discharge processes.[49]

To further reveal the chemisorption and surface composition change, the ex situ C 1s XPS spectra were researched (Figure 5d,e). Obviously, a new peak of −C−O−Zn (288.0 eV) gradually enhance during discharge states, then the value returns to its original level when the potential gets back to 1.8 V, which concludes the existence of the reversible chemisorption between Zn^{2+} and hydroxyl groups during charge/discharge processes.[54,55] Synchronously, the ex-situ O 1s XPS spectra of PN-HOPC are curve-fitted by three component peaks of −C = O, −C−OH, and COOH.[12,56] Noticeably, the intensities of −C = O continuously reduce during the discharge process from 1.8 V (33.6%) to 0.2 V (19.8%) (Figure 5f). When PN-HOPC cathode is charged to 1.8 V, the percentage of -C = O can be gradually recovered to 34.1%, indicating that partial −C−OH participates in oxidizing reaction into -C = O during the charge process, and -C = O could reversibly reduce back to −C−OH during the discharge process. The aforementioned results demonstrate that the oxygen functional groups not only facilitate ion and electron transports but also effectively offer additional chemical adsorption for

Zn^{2+} storage. Moreover, the ex-situ N 1s XPS spectra (Figure 5g) of PN-HOPC can be assigned to pyridinic N, pyrrolic N, graphitic N, and oxidized N. The pyridinic N signal gradually decreases during the discharge process (A to D) due to the enhanced adsorption of Zn^{2+} and reversibly increase during the charge process (D to G) owing to the removal of Zn^{2+} from the electroactive sites.[52] Meanwhile, the peak intensities of oxidized N gradually increase during the discharge state and then reduce during the charging state, revealing that the pyridinic N group can stimulate the uptake capability of Zn^{2+}.

In situ EQCM technique was further conducted to investigate the mass change of cathode during the whole charge and discharge processes. The mass change profile shows the obvious differences in ion species and numbers of ion adsorption (Figure 5h). The Faraday's law was employed to evaluate the molar mass (M/z) and determine the adsorption/desorption of ion species and the solvation numbers.[57,58] The M/z of the adsorbed ions calculated from the experimental slope is 1438.3 g mol^{-1} in region a, (Figure 5i), which is assigned to 2 $Zn_4SO_4(OH)_6·5H_2O$ (549.7 g mol^{-1}) precipitation, 12 H^+ (1 g mol^{-1}) adsorption, and 5 Zn^{2+} (65.4 g mol^{-1}) adsorption. Furthermore, the $M/z = 67.8$ g mol^{-1} in region b is nearly equal to 4 Zn^{2+} (65.4 g mol^{-1}) adsorption and 2 SO_4^{2-} (96.1 g mol^{-1}) desorption. Moreover, $M/z = 1469.7$ g mol^{-1} was obtained for region c (Figure 5j), which is consistent with 2 $Zn_4SO_4(OH)_6·5H_2O$ invertible dissolution, 11 H^+ desorption, and 5.5 Zn^{2+} reversible desorption. Consequently, the EQCM tests confirm that the charge storage mechanism of PN-HOPC cathode in ZICs mainly constitutes of the Zn^{2+}, H^+, and SO_4^{2-} co-adsorption, accompanying with the reversible precipitation/dissolution of $Zn_4SO_4(OH)_6·5H_2O$ byproduct, which well agrees with ex situ characterizations. The formation process of $Zn_4SO_4(OH)_6·5H_2O$ flakes is attributed to the concentrations of Zn^{2+}, OH^- and SO_4^{2-}, and the pH variation of electrolyte is an important indicator to affect the precipitation of $Zn_4SO_4(OH)_6·5H_2O$, suggesting that the H^+ participated in the electrochemical reactions process.[57] Simultaneously, the H^+ adsorption of the PN-HOPC electrode would expedite the transformation of −C = O group into C−OH group, and eventually generate the −C−O−Zn. In addition, the adsorption of H^+ can boost the $Zn_4SO_4(OH)_6·5H_2O$ precipitation and benefit for the transformation of oxygen functional groups. Specifically, in situ Raman spectra further confirm that the defect degrees of PN-HOPC electrode were enhanced after discharge process, corresponding to the Zn^{2+}/H^+ cations adsorption on the carbon surface (Figure 5k).

In combination of the systemic ex situ analysis and in situ Raman and EQCM techniques, the energy storage mechanism of the PN-HOPC cathode can be schematically speculated in Figure 5l. The excellent capacity of PN-HOPC cathode is achieved by coupling multiple charge storage mechanisms of electric double-layer capacitance (EDLC) as well as reversible hydrogen and oxygen redox reactions. First, the Zn^{2+}, H^+, and SO_4^{2-} co-adsorption was revealed during the charge storage process. In detail, the adsorption/desorption of Zn^{2+} and H^+ cations mainly took place at low voltages while the adsorption/desorption of SO_4^{2-} anions mainly happened at high voltages. Second, P, N co-doping could decrease the energy barrier of the Zn^{2+} absorption and optimizes electron/ion transport behaviors. Meanwhile, the invertible chemical adsorption of oxygen functional groups

**ADVANCED
SCIENCE NEWS**

www.advancedsciencenews.com

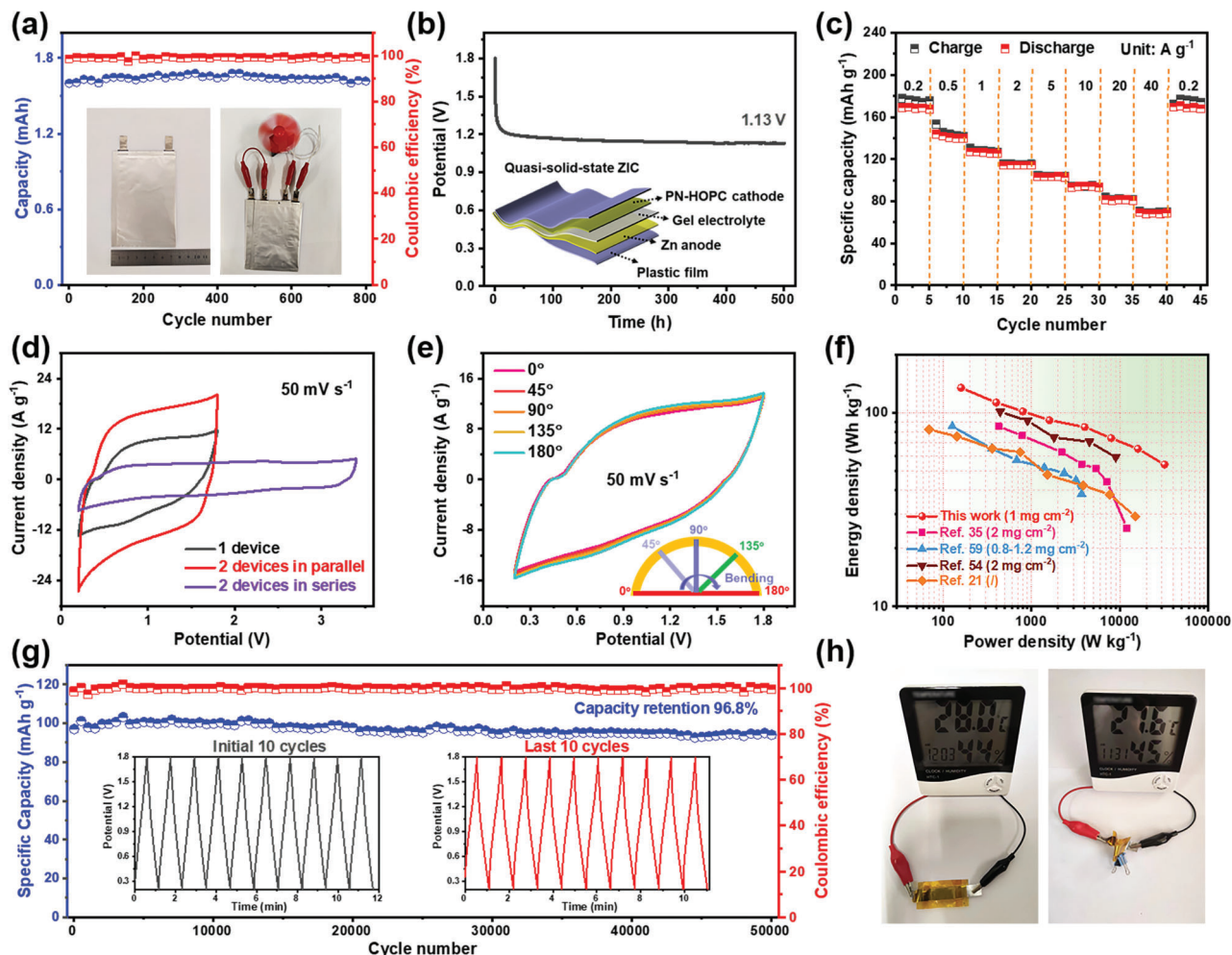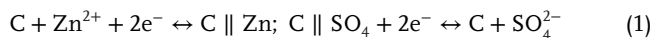**ADVANCED
FUNCTIONAL
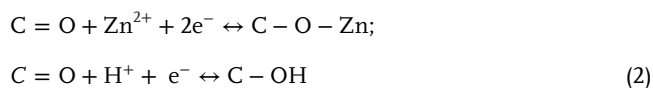MATERIALS**

www.afm-journal.de

Figure 6. a) Cycling capability of the pouch-cell ZIC. Inset picture is the assembled pouch-cell ZIC. Performance of quasi-solid-state ZIC: b) Self-discharge curve (inset diagram is the structure of quasi-solid-state ZIC). c) Rate performance. d) CV curves of ZICs in single, parallel and series. e) CV curves at different bending angles. f) Comparison of energy/power densities of quasi-solid-state ZIC with recent reported devices. g) Long-term cycling capability at 10 A g⁻¹. h) Photograph records of a device powered thermo-hygrometer.
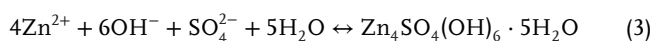
also was participated in the charge/discharge processes to form the −C−O−Zn, providing enhanced chemical adsorption and excellent capacitive performance. Third, the $Zn_4SO_4(OH)_6\cdot5H_2O$ flakes reversible formation/dissolution was ascribed to the adsorption/desorption of H^+ during the charge storage process. The charge storage process of PN-HOPC//Zn ZIC could be described as follows: (1) Physical adsorption/desorption:

$$C + Zn^{2+} + 2e^- \leftrightarrow C \parallel Zn;\ C \parallel SO_4 + 2e^- \leftrightarrow C + SO_4^{2-} \quad (1)$$

Chemical adsorption/desorption:

$$C = O + Zn^{2+} + 2e^- \leftrightarrow C - O - Zn;$$

$$C = O + H^+ + e^- \leftrightarrow C - OH \quad (2)$$

Precipitation/dissolution:

$$4Zn^{2+} + 6OH^- + SO_4^{2-} + 5H_2O \leftrightarrow Zn_4SO_4(OH)_6 \cdot 5H_2O \quad (3)$$

To verify the practical application of PN-HOPC based ZIC, the pouch cells and quasi-solid-state ZICs were further constructed. The pouch cell can show a high capacity of 1.62 mAh at a discharge current of 50 mA, and can work well throughout 800 charging/discharging cycles (**Figure 6**a). As a proof-of-concept demonstration, two pouch cells connected in series can successfully power an electric fan. Interestingly, the self-discharge performance of quasi-solid-state ZIC was studied after full-charge to 1.8 V. As shown in Figure 6b, the quasi-solid-state ZIC exhibits a rapid self-discharge rate in the initial stage, which saturates around 1.2 V after self-discharge 24 h. After 500 h of self-discharge, the potential of 1.13 V is maintained, indicating that the quasi-solid-state ZIC has outstanding anti-self-discharge ability. Specifically, the quasi-solid-state ZIC exhibits admirable Zn^{2+} storage capabilities, including a superb capacity of 168.5 mAh g⁻¹ at 0.2 A g⁻¹, and an exceptional rate performance (67.7 mAh g⁻¹ even at 40 A g⁻¹) (Figure 6c; Figure S32, Supporting Information). Meanwhile, the current and operating voltage can be boosted through linking the as-assembled ZICs in parallel and

series (Figure 6d). Besides, the quasi-solid-state ZIC also exhibits remarkable flexibility. Remarkably, the CV curves remained great superpositions when the ZIC bent under various angles from 0° to 180° (Figure 6e). Significantly, the quasi-solid-state ZIC offers a superior energy density of 134.8 Wh kg^{-1} and a maximal power density of 32.0 Kw kg^{-1}, which is superior to most reported ZICs[21,35,54,59] (Figure 6f). More encouragingly, the quasi-solid-state ZIC demonstrates a high capacity of 97.1 mAh g^{-1} at 10 A g^{-1} and an excellent cycling life with 96.8% capacity retention after 50 000 cycles (Figure 6g). Moreover, a thermo-hygrometer was easily driven by a single device (Figure 6h), which proves that the PN-HOPC based ZIC is promising next-generation energy storage devices for practical applications.

3. Conclusion

In summary, the Zn^{2+} storage capability of PN-HOPC was enhanced via eliminating the micropore confinement effect and introducing multiple chemisorption sites. The optimized PN-HOPC with matchable pore size, abundant zinc storage sites and rich heteroatom (P, N, O) doping could achieve efficient Zn^{2+} storage. In addition, DFT calculation showed that the P and N co-doping significantly contribute to the reversible adsorption/desorption of zinc ions and protons, and markedly reduce the energy barrier of the Zn^{2+} absorption. Consequently, the as-fabricated ZIC displays satisfactory Zn^{2+} storage capabilities with high capacity of 211.9 mAh g^{-1}, large-current survivability (80 A g^{-1}), superb energy density (169.5 Wh kg^{-1}), and ultralong-term cycling durability to 60 000 cycles. Simultaneously, the systematic ex-situ tests integrating with in situ Raman spectroscopy and EQCM techniques reveal that the exceptional electrochemical property is due to the synergic effect of the Zn^{2+}, H$^+$, and SO$_4^{2-}$ co-adsorption mechanism as well as reversible chemical adsorption, accompanying with the Zn$_4$SO$_4$(OH)$_6$·5H$_2$O reversible formation/dissolution. Moreover, the quasi-solid-state ZIC is assembled with landmark energy density, long cycle life of 50 000 cycles, and excellent mechanical property. Thereby, this work not only reports an enlightening insight for boosting the Zn^{2+} storage capabilities of carbon materials, but also provides light on the fundamental understanding of energy storage mechanism for high-performance ZICs design.

Supporting Information

Supporting Information is available from the Wiley Online Library or from the author.

Acknowledgements

Conflict of Interest

The authors declare no conflict of interest.

[1] Z. Zhu, T. Jiang, M. Ali, Y. Meng, Y. Jin, Y. Cui, W. Chen, *Chem. Rev.* **2022**, *122*, 16610.

[2] M. R. Lukatskaya, B. Dunn, Y. Gogotsi, *Nat. Commun.* **2016**, *7*, 12647.

[3] R. Fei, H. Wang, Q. Wang, R. Qiu, S. Tang, R. Wang, B. He, Y. Gong, H. J. Fan, *Adv. Energy Mater.* **2020**, *10*, 2002741.

[4] M. Peng, L. Wang, L. Li, Z. Peng, X. Tang, T. Hu, K. Yuan, Y. Chen, *eScience* **2021**, *1*, 83.

[5] W. Ye, X. Li, B. Zhang, W. Liu, Y. Cheng, X. Fan, H. Zhang, Y. Liu, Q. Dong, M. S. Wang, *Adv. Mater.* **2023**, *35*, 2210447.

[6] W. Liu, H. Zhang, W. Ye, B. Xiao, Z. Sun, Y. Cheng, M. S. Wang, *Small* **2023**, https://doi.org/10.1002/smll.202300605e2300605.

[7] J. Chen, Y. Cheng, Q. Zhang, C. Luo, H. Y. Li, Y. Wu, H. Zhang, X. Wang, H. Liu, X. He, J. Han, D. L. Peng, M. Liu, M. S. Wang, *Adv. Funct. Mater.* **2021**, *31*, 2007158.

[8] L. Li, Q. Zhang, B. He, R. Pan, Z. Wang, M. Chen, Z. Wang, K. Yin, Y. Yao, L. Wei, L. Sun, *Adv. Mater.* **2022**, *34*, 2104327.

[9] H. Zhang, X. Liu, H. Li, I. Hasa, S. Passerini, *Angew. Chem., Int. Ed.* **2020**, *60*, 598.

[10] H. Ma, H. Chen, Y. Hu, B. Yang, J. Feng, Y. Xu, Y. Sun, H. Cheng, C. Li, X. Yan, L. Qu, *Energy Environ. Sci.* **2022**, *15*, 1131.

[11] Z. Peng, S. Li, Y. Huang, J. Guo, L. Tan, Y. Chen, *Adv. Funct. Mater.* **2022**, *32*, 2206539.

[12] J. Yin, W. Zhang, W. Wang, N. A. Alhebshi, N. Salah, H. N. Alshareef, *Adv. Energy Mater.* **2020**, *10*, 2001705.

[13] B. Zakeri, S. Syri, *Renew. Sustain. Energy Rev.* **2015**, *42*, 569.

[14] J. Yin, W. Zhang, N. A. Alhebshi, N. Salah, H. N. Alshareef, *Adv. Energy Mater.* **2021**, *11*, 2100201.

[15] H. Tang, J. Yao, Y. Zhu, *Adv. Energy Mater.* **2021**, *11*, 2003994.

[16] D. Han, Z. Wang, H. Lu, H. Li, C. Cui, Z. Zhang, R. Sun, C. Geng, Q. Liang, X. Guo, Y. Mo, X. Zhi, F. Kang, Z. Weng, Q.-H. Yang, *Adv. Energy Mater.* **2022**, *12*, 2102982.

[17] F. Wang, O. Borodin, T. Gao, X. Fan, W. Sun, F. Han, A. Faraone, J. A. Dura, K. Xu, C. Wang, *Nat. Mater.* **2018**, *17*, 543.

[18] H. Tian, J.-L. Yang, Y. Deng, W. Tang, R. Liu, C. Xu, P. Han, H. J. Fan, *Adv. Energy Mater.* **2022**, *13*, 2202603.

[19] Z. Peng, J. Guo, Q. He, S. Li, L. Tan, Y. Chen, *Sci. China Mater.* **2022**, *65*, 2401.

[20] H. Wang, M. Wang, Y. Tang, *Energy Storage Mater.* **2018**, *13*, 1.

[21] L. Dong, X. Ma, Y. Li, L. Zhao, W. Liu, J. Cheng, C. Xu, B. Li, Q.-H. Yang, F. Kang, *Energy Storage Mater.* **2018**, *13*, 96.

[22] Z. Li, D. Chen, Y. An, C. Chen, L. Wu, Z. Chen, Y. Sun, X. Zhang, *Energy Storage Mater.* **2020**, *28*, 307.

[23] W. Zhang, J. Yin, W. Jian, Y. Wu, L. Chen, M. Sun, U. Schwingenschlögl, X. Qiu, H. N. Alshareef, *Nano Energy* **2022**, *103*, 107827.

[24] C. C. Hou, Y. Wang, L. Zou, M. Wang, H. Liu, Z. Liu, H. F. Wang, C. Li, Q. Xu, *Adv. Mater.* **2021**, *33*, 2101698.

ADVANCED
SCIENCE NEWS
www.advancedsciencenews.com

ADVANCED
FUNCTIONAL
MATERIALS
www.afm-journal.de

[25] J. Li, J. Zhang, L. Yu, J. Gao, X. He, H. Liu, Y. Guo, G. Zhang, *Energy Storage Mater.* **2021**, *42*, 705.

[26] W. Fan, J. Ding, J. Ding, Y. Zheng, W. Song, J. Lin, C. Xiao, C. Zhong, H. Wang, W. Hu, *Nano-Micro Lett.* **2021**, *13*, 59.

[27] G. Sun, H. Yang, G. Zhang, J. Gao, X. Jin, Y. Zhao, L. Jiang, L. Qu, *Energy Environ. Sci.* **2018**, *11*, 3367.

[28] G. Nagaraju, S. Tagliaferri, A. Panagiotopoulos, M. Och, R. Quintin-Baxendale, C. Mattevi, *J. Mater. Chem. A* **2022**, *10*, 15665.

[29] S. W. Chen, Y. Chen, T. Jiao, J. Zhou, J. Cheng, B. Liu, S. Yang, K. Zhang, W. Zhang, *Adv. Energy Mater.* **2019**, *9*, 1902915.

[30] H. Xu, W. He, Z. Li, J. Chi, J. Jiang, K. Huang, S. Li, G. Sun, H. Dou, X. Zhang, *Adv. Funct. Mater.* **2022**, *32*, 2111131.

[31] J. Luo, L. Xu, H. Liu, Y. Wang, Q. Wang, Y. Shao, M. Wang, D. Yang, S. Li, L. Zhang, Z. Xia, T. Cheng, Y. Shao, *Adv. Funct. Mater.* **2022**, *32*, 2112151.

[32] M. Hartmann, T. Clark, R. van Eldik, *J. Am. Chem. Soc.* **1997**, *119*, 7843.

[33] E. R. Nightingale, *J. Phys. Chem.* **1959**, *63*, 1381.

[34] H. Ma, H. Chen, M. Wu, F. Chi, F. Liu, J. Bai, H. Cheng, C. Li, L. Qu, *Angew. Chem., Int. Ed.* **2020**, *59*, 14541.

[35] Y. Lu, Z. Li, Z. Bai, H. Mi, C. Ji, H. Pang, C. Yu, J. Qiu, *Nano Energy* **2019**, *66*, 104132.

[36] Y. Li, J. Huang, L. Kang, Z. Tian, F. Lai, D. J. L. Brett, T. Liu, G. He, *Sci. China Mater.* **2022**, *65*, 1495.

[37] H. He, J. Lian, C. Chen, Q. Xiong, C. C. Li, M. Zhang, *Nano-Micro Lett.* **2022**, *14*, 106.

[38] R. Yuksel, O. Buyukcakir, P. K. Panda, S. H. Lee, Y. Jiang, D. Singh, S. Hansen, R. Adelung, Y. K. Mishra, R. Ahuja, R. S. Ruoff, *Adv. Funct. Mater.* **2020**, *30*, 1909725.

[39] J. Li, L. Yu, W. Wang, X. He, G. Wang, R. Liu, X. Ma, G. Zhang, *J. Mater. Chem. A* **2022**, *10*, 9355.

[40] A. Amiri, M. Naraghi, A. A. Polycarpou, *J. Energy Chem.* **2022**, *70*, 480.

[41] Y.-L. Wu, X. Li, Y.-S. Wei, Z. Fu, W. Wei, X. T. Wu, Q.-L. Zhu, Q. Xu, *Adv. Mater.* **2021**, *33*, 2006965.

[42] Y. He, S. Hwang, D. A. Cullen, M. A. Uddin, L. Langhorst, B. Li, S. Karakalos, A. J. Kropf, E. C. Wegener, J. Sokolowski, M. Chen, D. Myers, D. Su, K. L. More, G. Wang, S. Litster, G. Wu, *Energy Environ. Sci.* **2019**, *12*, 250.

[43] X. Zhou, L. Chen, W. Zhang, J. Wang, Z. Liu, S. Zeng, R. Xu, Y. Wu, S. Ye, Y. Feng, X. Cheng, Z. Peng, X. Li, Y. Yu, *Nano Lett.* **2019**, *19*, 4965.

[44] X. Hu, G. Zhong, J. Li, Y. Liu, J. Yuan, J. Chen, H. Zhan, Z. Wen, *Energy Environ. Sci.* **2020**, *13*, 2431.

[45] P. Zhang, Y. Li, G. Wang, F. Wang, S. Yang, F. Zhu, X. Zhuang, O. G. Schmidt, X. Feng, *Adv. Mater.* **2019**, *31*, 1806005.

[46] X. Deng, J. Li, Z. Shan, J. Sha, L. Ma, N. Zhao, *J. Mater. Chem. A* **2020**, *8*, 11617.

[47] Z. Wang, J. Huang, Z. Guo, X. Dong, Y. Liu, Y. Wang, Y. Xia, *Joule* **2019**, *3*, 1289.

[48] T. Brezesinski, J. Wang, S. H. Tolbert, B. Dunn, *Nat. Mater.* **2010**, *9*, 146.

[49] X. Li, Y. Li, X. Zhao, F. Kang, L. Dong, *Energy Storage Mater.* **2022**, *53*, 505.

[50] P. L. Taberna, P. Simon, J. F. Fauvarque, *J. Electrochem. Soc.* **2003**, *150*, A292.

[51] H. Zhang, Q. Liu, Y. Fang, C. Teng, X. Liu, P. Fang, Y. Tong, X. Lu, *Adv. Mater.* **2019**, *31*, 1904948.

[52] Z. Song, L. Miao, L. Ruhlmann, Y. Lv, D. Zhu, L. Li, L. Gan, M. Liu, *Adv. Funct. Mater.* **2022**, *32*, 2208049.

[53] X. Zhang, Y. Zhang, J. Qian, Y. Zhang, L. Sun, Q. Wang, *Nanoscale* **2022**, *14*, 2004.

[54] H. Fan, X. Hu, S. Zhang, Z. Xu, G. Gao, Y. Zheng, G. Hu, Q. Chen, T. S. AlGarni, R. Luque, *Carbon* **2021**, *180*, 254.

[55] Y. Shao, Z. Sun, Z. Tian, S. Li, G. Wu, M. Wang, X. Tong, F. Shen, Z. Xia, V. Tung, J. Sun, Y. Shao, *Adv. Funct. Mater.* **2021**, *31*, 2007843.

[56] X. Zheng, L. Miao, Z. Song, W. Du, D. Zhu, Y. Lv, L. Li, L. Gan, M. Liu, *J. Mater. Chem. A* **2022**, *10*, 611.

[57] L. Liu, Y. C. Wu, L. Huang, K. Liu, B. Duployer, P. Rozier, P.-L. Taberna, P. Simon, *Adv. Energy Mater.* **2021**, *11*, 2101287.

[58] M. Salanne, B. Rotenberg, K. Naoi, K. Kaneko, P.-L. Taberna, C. P. Grey, B. Dunn, P. Simon, *Nat. Energy* **2016**, *1*, 16070.

[59] Y. Zheng, W. Zhao, D. Jia, Y. Liu, L. Cui, D. Wei, R. Zheng, J. Liu, *Chem. Eng. J.* **2020**, *387*, 124161.